PHYSICAL REVIEW B **83**, 195322 (2011)

Strain-driven formation of rubrene crystalline films on Bi(001)

Meng Lan,[1] Zu-Hong Xiong,[1] Guo-Qing Li,[1] Ting-Na Shao,[1] Jia-Le Xie,[1] Xiu-Fan Yang,[1] Jun-Zhong Wang,[1,*] and Ying Liu[2,†]
[1]*School of Physical Science and Technology & MOE Key Laboratory on Luminescence and Real-Time Analysis, Southwest University, Chongqing 400715, People's Republic of China*
[2]*Department of Physics and Hebei Advanced Thin Film Laboratory, Hebei Normal University, Shijiazhuang 050016, Hebei, People's Republic of China*

(Received 16 November 2010; revised manuscript received 8 February 2011; published 25 May 2011)

We report the formation of rubrene crystalline films on Bi(001) substrate starting from the very first layer. With coverage increasing, rubrene shows a structural evolution from self-assembled monolayer to a composite phase, which consists of rubrene crystalline domains and self-assembled domain walls. In particular, Kurdjunov-Sachs (KS) rotational epitaxy has been found in rubrene crystalline domains, which reveal large compressive strains. Further deposition of rubrene leads to a layer-by-layer growth of crystalline films up to the fourth layer. The driving force for rubrene crystallinity in the monolayer regime has been attributed to the anisotropic strains generated in KS rotation epitaxy.

DOI: 10.1103/PhysRevB.83.195322 PACS number(s): 68.55.am, 61.66.Hq, 68.35.bm, 68.37.Ef

I. INTRODUCTION

The organic semiconductor has significant applications in microelectronic devices such as organic light emitting diodes (OLEDs) and organic field effect transistors (OFETs).[1–5] Since charge transports depend strongly on the lateral ordering and crystallinity degree at the molecule-substrate interface, it is necessary to fabricate organic crystalline films starting from the first monolayer. However, as most organic molecules exhibit shape anisotropy and additional degrees of freedom, the molecular orientation and conformation may change during growth, introducing additional sources of disorder.

Rubrene ($C_{42}H_{28}$), comprised of a tetracene backbone and four phenyl side groups, has been recently identified as a promising material due to the efficient luminescence and high charge-carrier mobility. OFETs made of rubrene single crystals reveal a very high carrier mobility ($\sim$15 cm^2/Vs).[6,7] Nevertheless, it is difficult to produce rubrene-based OFETs with satisfactory electronic properties, due to the inablility to grow rubrene epitaxial films by organic molecular-beam deposition (OMBD). Käfer *et al.* studied the fundamental mechanism that limits the epitaxy growth of rubrene.[8] They demonstrated that the tetracene backbones of rubrene molecules remains twisted upon deposition of the first few monolayers, whereas it becomes planar at higher coverage. As a consequence, the first monolayers of rubrene are disordered, hindering further formation of crystalline films. Density function theory (DFT) calculations reveal that the free rubrene molecule has a twisted ($\sim$42°) tetracene backbone, leading to an axial chirality as shown in Fig. 1(a), while the rubrene crystals adopt a planar tetracene backbone without any chirality.[9]

Recently there has been tremendous effort in growing rubrene crystalline thin films on various substrates. Nevertheless, a lot of self-assembled monolayer (SAM) or supramolecular structures have been obtained on noble-metal substrates like Au,[10–14] Cu,[9,15,16] and Ag.[17] For thick rubrene films, amorphous or polycrystalline rubrene films formed upon deposition onto muscovite,[18] SiO_2 without[19] or with buffer layers.[20,21] Multilayer rubrene islands with a rectangular lattice distinct from the *a*-*b* plane of rubrene crystal have been found on Au(111).[22] In particular, thick rubrene films with crystalline orientation have been obtained by special solution processing[23] or by hot wall deposition on Au(111).[24] Atomic force microscopy (AFM) measurements indicated a step height close to the *d* spacing of the *a*-*b* plane in rubrene crystals. However, it is not clear about the in-plane structure as well as the crystallinity degree near molecule-substrate interface. Thus growth of rubrene crystalline films on appropriate substrates starting from the first monolayer remains still a big challenge.

It was reported recently that pentacene, another benchmark molecule, grown on the semimetallic Bi(001) substrate forms the epitaxial crystalline films with pentacene molecule standing up, even in the first monolayer.[25,26] The upright orientation of the pentacene molecule is attributed to the small density of states near the Fermi level, which leads to the reduction of molecule-substrate interaction.[27] In this paper, we demonstrate the formation of rubrene crystalline films on Bi(001) starting from the molecule-substrate interface. A composite phase consisting of rubrene crystalline domains and self-assembled domain walls has been observed in the first monolayer. Afterwards, the layer-by-layer growth of rubrene crystalline films has been found to persist up to the fourth monolayer. The crystallinity of rubrene molecules in the monolayer regime has been attributed to the large strains resulting from Kurdjunov-Sachs (KS) rotation epitaxy.[28,29]

II. EXPERIMENT

The experiments were performed in an ultrahigh vacuum low-temperature scanning tunnel microscope (STM) (Unisoku) with the base pressure $\sim 1.2 \times 10^{-10}$ mbar. Bi(001) thin film was prepared by depositing 20-monolayer (ML) Bi on Si(111)-7×7 at room temperature (RT) with subsequent annealing at $\sim$120 °C. Rubrene molecules (Aldrich, purity 99%) were grown at RT from a quartz Knudsen cell heated to $\sim$200 °C. The typical growth rate was about 0.03 ML per minute. Throughout this paper we define rubrene coverage in terms of crystalline monolayer (ML) corresponding to the *a*-*b* plane in rubrene crystals. In order to establish the adsorption model of the rubrene molecule, spin-polarized DFT

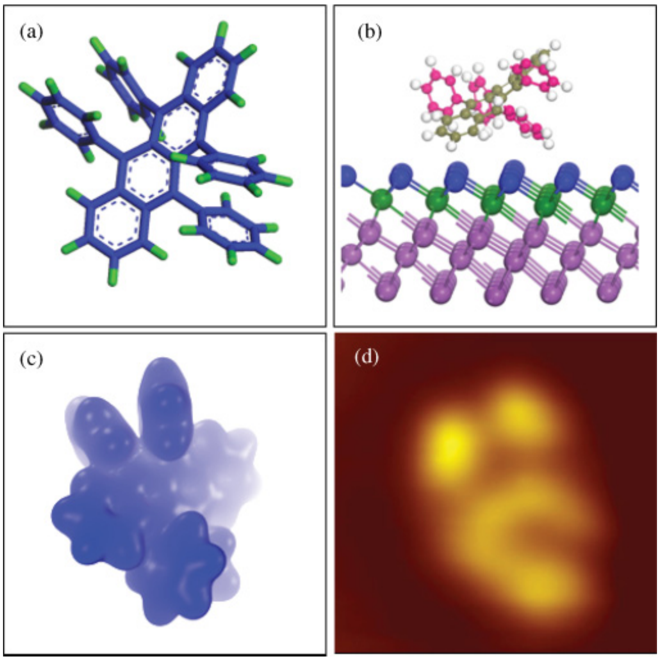

FIG. 1. (Color online) (a) Schematic structure of the free rubrene molecule. (b) Side view of the optimized adsorption model of rubrene on Bi(001). The atoms within the top two layers of Bi substrate are labeled by different colors. (c) Top view of the calculated total electron density for the optimized rubrene molecule. (d) STM image of singular rubrene molecule adsorbed on Bi(001), 3 nm × 3 nm, 2.0 V.

geometric optimization with the generalized gradient approximation (GGA) has been performed. The gradient corrected Perdew-Wang 91 exchange-correlation functional and double-numerical polarized basis were employed.[30] Figure 1(b) shows the side view of the optimized geometry of a rubrene molecule adsorbed on the Bi(001) surface, where the long axis of the tetracene backbone exhibits a 29.8° angle with respect to the substrate plane, and the closest molecule-substrate distance is 2.5 Å. Figure 1(c) is the top view of the calculated total electronic density of the rubrene molecule. It is consistent with the experimental STM image displayed in Fig. 1(d), where the rubrene molecule reveals five protrusions.

III. EXPERIMENTAL RESULTS

When deposited on Bi(001), rubrene molecules are initially self-assembled into monolayer islands, which prefer to stick to the step edges of the Bi substrate; Fig. 2(a). On the complete layer of rubrene SAM, a moiré pattern characterized by a 4 × 3 supercell has been observed; Fig. 2(b). The lattice constants of rubrene SAM are $c_1 = 14.6 \pm 0.2$ Å, $c_2 = 16.6 \pm 0.2$ Å, $\theta = 68.0 \pm 0.5^\circ$, and c_1 is parallel to a principal axis of Bi(001). The packing density is calculated to be ~ 0.89 nm^{-2}. Based on the moiré pattern and the lattice constant of the Bi(001) surface ($a_1 = a_2 = 4.54$ Å),[31] the SAM lattice vectors can be expressed as

$$\begin{pmatrix} c_1 \\ c_2 \end{pmatrix} = \begin{pmatrix} 13/4 & 0 \\ -2/3 & 4 \end{pmatrix} \begin{pmatrix} a_1 \\ a_2 \end{pmatrix}. \qquad (1)$$

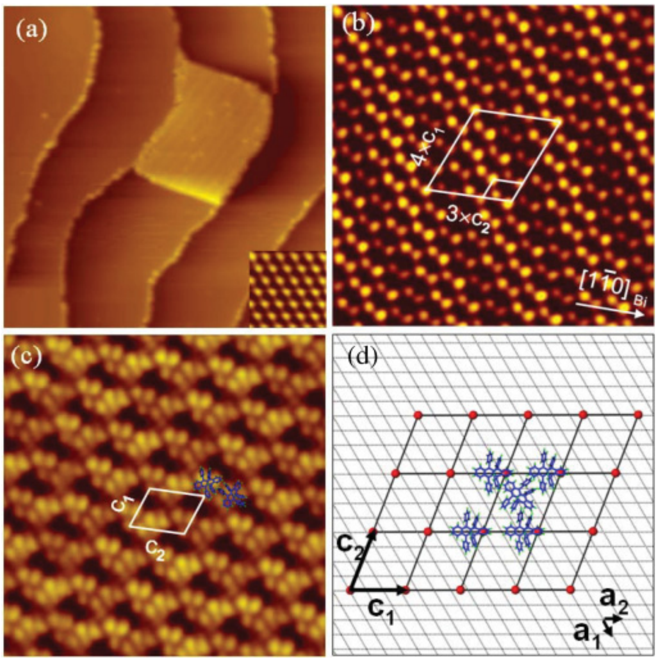

FIG. 2. (Color online) STM images for the self-assembled monolayer (SAM) of rubrene formed on Bi(001). (a) A self-assembled rubrene island sticking to the step edges of substrate, 135 nm × 135 nm, 2.0 V. Inset is atomic-resolution STM image of Bi(001) surface. (b) The SAM of rubrene formed at ~0.4 ML, with a moiré pattern characterized by 4 × 3 supercell, 20 nm × 20 nm, 2.5 V. (c) High-resolution STM image acquired on the rubrene SAM, 10 nm × 10 nm, 3.5 V. (d) Schematic diagram for the point-on-line coincidence orientation of rubrene SAM on Bi(001).

The presence of two integers in the single column of the transformation matrix reveals a point-on-line coincident relation between rubrene SAM and Bi(001).[32] From the high-resolution STM image in Fig. 2(c), we noticed that each unit cell includes two inequivalent molecules: one manifests three protrusions similar to the molecular image in supramolecular structures,[10] the other exhibits five protrusion lobes, similar to the molecular image in Fig. 1(d). Thus we speculate that each molecule in rubrene SAM adopts an essentially lying-down orientation on Bi(001). Figure 2(d) is the schematic diagram for the structural model of rubrene SAM, where all the molecular lattice points reside on the substrate lattice lines along the a_2 axis (point on line).

Upon further increasing the rubrene coverage, it is found that rubrene SAM transforms into a composite phase, which corresponds to a collection of rubrene crystalline domains separated by domain walls. Figure 3(a) shows the derivative of the topographic STM image for the rubrene composite phase, in order to enhance the appearance of surface features. It is noticed that the domain walls exhibit zigzag patterns with parallel alignments. From the close-up view in Fig. 3(b), we noticed that the domain walls are aligned along either the $[\bar{1}\bar{1}2]$ or $[1\bar{2}1]$ direction of Bi(001). From the high-resolution STM image in Fig. 3(c), it is observed that the domain walls have a hexagonal lattice ($c = 15.5 \pm 0.1$ Å), which is $2\sqrt{3} \times 2\sqrt{3}$ reconstructed with Bi(001). Within the crystalline domains, a rectangular lattice with herringbone molecule

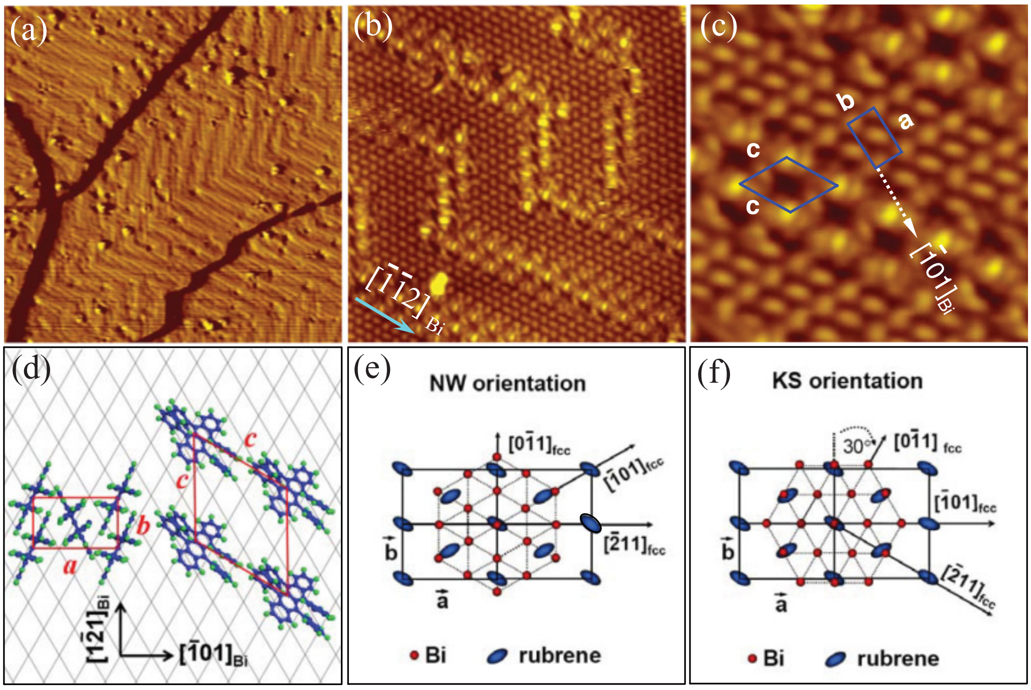

FIG. 3. (Color online) Rubrene composite phase formed on Bi(001) at ~0.7 ML. (a) Derivative of the topographic STM image for the rubrene composite phase, 100 nm × 100 nm, 4.5 V. (b) STM image of rubrene composite phase shows clearly the alignments of domain walls, 25 nm × 25 nm, 2.5 V. (c) High-resolution STM image of the rubrene composite phase, 9 nm × 9 nm, 2.5 V. (d) Schematic illustration for the structural model of rubrene composite structure. (e) and (f) show the Nishiyama-Wassermann (NW) and Kurdjumov-Sachs (KS) orientation relationships between the quasi-bcc(110) lattice of crystalline rubrene and fcc(111) substrate, respectively.

packing has been identified. The lattice constants are a = 12.6 ± 0.1 Å, b = 7.3 ± 0.1 Å, very close to those of the a-b plane in rubrene crystals [a_0 = 14.4 Å, b_0 = 7.2 Å (Ref. 33)]. Thus this rubrene crystalline phase corresponds to a strained a-b plane of rubrene crystal. The molecular packing density is 2.2 nm^{-2}, which is 2.5 times that of rubrene SAM. By calculating the transformation matrix, we realized that this crystalline phase is incommensurate with Bi(001). We noticed that this crystalline phase exhibits a similar in-plane structure as the thick crystalline films of rubrene obtained by solution processing[23] or hot wall deposition.[24] However, their crystallization methods are different. Our crystalline rubrene phase was formed in the monolayer regime, while it is not clear about the crystallinity degree near the molecule-substrate interface for the thick crystalline films mentioned above. Here we define the anisotropic strain as the fractional deviation of each lattice constant from the bulk value, thus $\delta_a = (a - a_0)/a_0 = -12.5\%$, $\delta_b = (b - b_0)/b_0 = 1.4\%$. It means that a large compressive strain builds up in the rubrene crystalline phase. Furthermore, this strain is highly anisotropic ($\delta_a > \delta_b$). In addition, we noticed that one c-axis of the domain walls is parallel to the a-axis of crystalline phase, while the a-axis and b-axis of crystalline phase are parallel to the $[\bar{1}01]$ and $[1\bar{2}1]$ directions of Bi(001), respectively. The structural model for the rubrene composite phase is shown in Fig. 3(d). Interestingly, it is observed that the a and b axes constitute a right-angle triangle with an angle of 30.1°, which matches precisely the hexagonal lattice of Bi(001). Thus we can say the lattice alignment of the rubrene crystalline phase is "locked in" by the hexagonal lattice of Bi(001) in spite of the incommensurism.

In fact, a similar orientational relationship was found in the bcc(110)/fcc(111) system.[28,29,34] In Nishiyama-Wassermann (NW) orientation, the b axis of bcc(110) is parallel to a principal axis of the fcc(111) lattice; Fig. 3(e). If the rubrene crystalline phase adopts this orientation, the lattice misfit would be $m_{\text{NW}} = 19.8\%$, which is too large to be favored. In the KS orientation, the fcc(111) lattice rotates an angle of 30° such that the a axis of bcc(110) is parallel to a principal axis of fcc (111); Fig. 3(f). If the rubrene crystalline phase adopts KS orientation, the lattice misfit will reduce significantly to $m_{\text{KS}} = 7.4\%$. Coincidently, we realized that the structural model of the rubrene crystalline phase shown in Fig. 3(d) is consistent with KS orientation. According to the analysis by Zangwill,[29] in KS rotational epitaxy, the incommensurate film achieves row matching only in an average sense. Coherence is lost through a complicated interplay of domain walls along one direction, and nonuniform strains in the other. This prediction is in agreement with our observation in the rubrene composite phase.

On the other hand, it seems that the formation of the crystalline rubrene layer in the first layer is surprising, since DFT calculation revealed that the energy difference between the twisted rubrene molecules in gas (or in thin films) and the planar molecules in crystals is 205 meV.[9] This means that, in order to realize the crystallinity of rubrene molecules in the monolayer regime, it requires an additional energy of ~205 meV to stabilize the planarization of the twisted backbone of the rubrene molecule. One may ask where

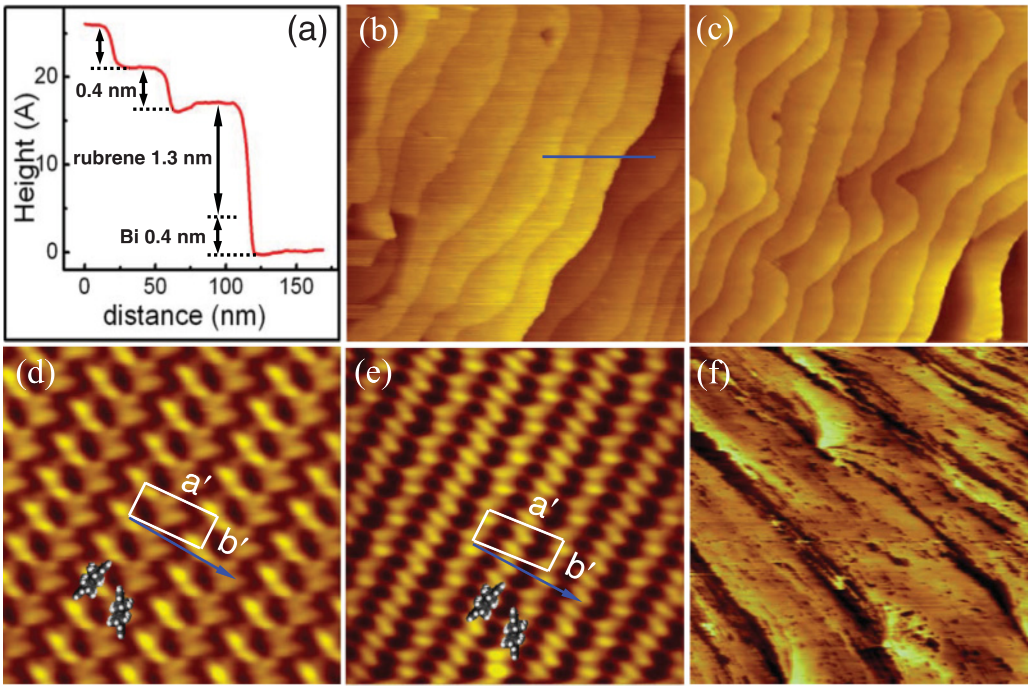

FIG. 4. (Color online) Subsequent layer-by-layer growth of rubrene crystalline layers on top of the composite phase. (a) Line scan corresponding to the blue line shown in (b). (b) STM image of a second layer rubrene island, 500 nm × 500 nm, 4.5 V. (c) STM image of the continuous second layer of rubrene formed at ∼1.5 MLs, 500 nm × 500 nm, 4.5 V. (d) and (e) are the high-resolution STM images acquired on the rubrene second layer with the bias of −4.0 V, and −2.0 V, respectively. The blue arrow is used to mark the direction of a principal axis of Bi(001), 6 nm × 6 nm. (f) Tapping-mode AFM image of the rubrene films with ∼4-ML thickness, 14 μm × 14 μm.

does this energy come from? The building up of the large compressive strain in the rubrene crystalline phase reminds us that this additional energy comes from the elastic strain energy generated in KS rotational epitaxy.

Upon further deposition of rubrene, layer-by-layer growth of rubrene crystalline layers has been observed. Figure 4(b) shows a second layer island of crystalline rubrene crossing several terraces. From the line scan shown in Fig. 4(a), we can distinguish the ∼1.3-nm step height associated with the *d* spacing of the *a*-*b* plane in rubrene crystals (1.35 nm), as well as the ∼0.4-nm step height of Bi(001) (the same as the step height of the rubrene composite phase due to the uniform covering). Figure 4(c) shows the morphology of the continuous second layer formed at ∼1.6 MLs. It is found that the morphology of the second rubrene layer is very smooth. In order to verify the two-dimensional growth mode, we scanned many places of the second rubrene layer. All of them exhibit the same lattice structure with the same orientation. Furthermore, we have also performed atomic force microscopy (AFM) scanning (∼15 μm) on the different regions of the sample surface. All the AFM images reveal smooth morphology of the second rubrene layer; no three-dimensional rubrene island and domain boundary have been found. Figures 4(d) and 4(e) show the bias-dependent STM images with submolecular resolution acquired on the second rubrene layer, where the top two phenyl side groups of the rubrene molecule can be resolved. Compared with the crystalline rubrene in the first layer, the lattice constant for the second rubrene layer reveal some modification: $a' = 13.8 \pm 0.1$ Å, $b' = 7.1 \pm 0.1$ Å. The anisotropic strains are reduced to $\delta'_a = -4.2\%$, $\delta'_b = -1.4\%$. Most importantly, we noticed a "lattice rotation" for the second rubrene layer: the a' axis of the second rubrene layer deviates the principal axis of Bi(001) for a small angle (∼5°). Thus we conclude that the lattice rotation of the second rubrene layer leads to a significant relief of strain. When the rubrene coverage is increased to 4 MLs, we found a transition from two- to three-dimensional growth, corresponding to the Stranski-Krastanov mode. However, due to the poor conductivity of multilayer rubrene, STM scanning becomes difficult even at very small tunneling current. In order to avoid the imaging artifacts, we perform tapping mode AFM measurements for 4 MLs of rubrene films; Fig. 4(f). It is found that the morphology of the multilayer rubrene is essentially smooth, except for some facet islands revealed by the bright protrusions. For higher coverage of rubrene films, AFM observation indicates that the film morphology becomes very rough.

IV. CONCLUSION

To summarize, crystalline rubrene films formed on the semimetallic Bi(001) substrate, even from the first monolayer. A composite phase consisting of rubrene crystalline domains and self-assembled domain walls appeared in the first rubrene layer. Most importantly, KS rotational epitaxy has been found in the rubrene crystalline domains. Further deposition of rubrene leads to a layer-by-layer growth of rubrene crystalline films up to the fourth layer. The driving force for rubrene crystallinity in the monolayer regime can be attributed to the large compressive strains resulting from KS rotational epitaxy.

ACKNOWLEDGMENTS

This work was supported by the National Natural Science Foundation of China (Grant No. 10974156), and the Natural Science Foundation Project of CQ CSTC (Grant No. 2008BB4003).

---

*jzwangcn@swu.edu.cn

†yliu@hebtu.edu.cn

[1] V. C. Sundar, J. Zaumseil, V. Podzorov, E. Menard, R. L. Willett, T. Someya, M. E. Gershenson, and J. A. Rogers, Science **303**, 1644 (2004).

[2] F.-J. M. z. Heringdorf, M. C. Reuter, and R. M. Tromp, Nature (London) **412**, 517 (2001).

[3] G. Witte and C. Wöll, Phys. Status Solidi **205**, 497 (2008).

[4] F. Schreiber, Phys. Status Solidi **201**, 1037 (2004).

[5] G. Witte and C. Wöll, J. Mater. Res. **19**, 1889 (2004).

[6] V. Podzorov, E. Menard, A. Borissov, V. Kiryukhin, J. A. Rogers, and M. E. Gershenson, Phys. Rev. Lett. **93**, 086602 (2004).

[7] R. Zeis, C. Besnard, T. Siegrist, C. Schlockmann, X. Chi, and C. Kloc, Chem. Mater. **18**, 244 (2006).

[8] D. Käfer, L. Ruppel, G. Witte, and C. Wöll, Phys. Rev. Lett. **95**, 166602 (2005).

[9] J. A. Miwa, F. Cicoira, S. Bedwani, J. Lipton-Duffin, D. F. Perepichka, A. Rochefort, and F. Rosei, J. Phys. Chem. C **112**, 10214 (2008).

[10] M. C. Blüm, E. Cavar, M. Pivetta, F. Patthey, and W. D. Schneider, Angew. Chem. Int. Ed. **117**, 5468 (2005).

[11] M. Pivetta, M. C. Blüm, F. Patthey, and W. D. Schneider, Angew. Chem. Int. Ed. **120**, 1092 (2008).

[12] M. C. Blüm, M. Pivetta, F. Patthey, and W. D. Schneider, Phys. Rev. B **73**, 195409 (2006).

[13] L. Wang, S. Chen, L. Liu, D. Qi, X. Gao, and A. T. S. Wee, Appl. Phys. Lett. **90**, 132121 (2007).

[14] L. Wang, H. Kong, X. Chen, X. Du, F. Chen, X. Liu, and H. Wang, Appl. Phys. Lett. **95**, 093102 (2009).

[15] F. Cicoira, J. A. Miwa, D. F. Perepichka, and F. Rosei, J. Phys. Chem. A **111**, 12674 (2007).

[16] J. A. Miwa, F. Cicoira, J. Lipton-Duffin, D. F. Perepichka, C. Santato, and F. Rosei, Nanotechnology **19**, 424021 (2008).

[17] M. Pivetta, M. C. Blüm, F. Patthey, and W. D. Schneider, Chem. Phys. Chem. **11**, 1558 (2010).

[18] T. Djuric, A. Thierry, W. Grogger, S. M. AbdAl-Baqi, H. Sitter, and R. Resel, Physica E (Amsterdam) **41**, 1718 (2009).

[19] S. Kowarik, A. Gerlach, S. Sellner, F. Schreiber, J. Pflaum, L. Cavalcantid, and O. Konovalovd, Phys. Chem. Chem. Phys. **8**, 1834 (2006).

[20] W. S. Hu, S. Z. Weng, Y. T. Tao, H. J. Liu, and H. Y. Lee, Org. Electron. **9**, 385 (2008).

[21] C. H. Hsu, J. Deng, C. R. Staddon, and P. H. Betona, Appl. Phys. Lett. **91**, 193505 (2007).

[22] M. Pivetta, M. C. Blum, F. Patthey, and W. D. Schneider, J. Phys. Chem. B **113**, 4578 (2009).

[23] N. Stingelin-Stutzmann, E. Smits, H. Wondergem, C. Tanase, P. Blom, P. Smith, and D. Deleeuw, Nat. Mater. **4**, 601 (2005).

[24] D. Käfer and G. Witte, Phys. Chem. Chem. Phys. **7**, 2850 (2005).

[25] J. T. Sadowski, T. Nagao, S. Yaginuma, Y. Fujikawa, A. Al-Mahboob, K. Nakajima, T. Sakurai, G. E. Thayer, and R. M. Tromp, Appl. Phys. Lett. **86**, 073109 (2005).

[26] G. E. Thayer, J. T. Sadowski, F. Meyer zu Heringdorf, T. Sakurai, and R. M. Tromp, Phys. Rev. Lett. **95**, 256106 (2005).

[27] H. Kakuta, T. Hirahara, I. Matsuda, T. Nagao, S. Hasegawa, N. Ueno, and K. Sakamoto, Phys. Rev. Lett. **98**, 247601 (2007).

[28] E. Bauer and J. H. van der Merwe, Phys. Rev. B **33**, 3657 (1986).

[29] A. Zangwill, *Physics at Surface* (Cambridge University Press, Cambridge, England, 1988).

[30] J. P. Perdew and Y. Wang, Phys. Rev. B **45**, 13244 (1992).

[31] T. Nagao, J. T. Sadowski, M. Saito, S. Yaginuma, Y. Fujikawa, T. Kogure, T. Ohno, Y. Hasegawa, S. Hasegawa, and T. Sakurai, Phys. Rev. Lett. **93**, 105501 (2004).

[32] D. E. Hooks, T. Fritz, and M. D. Ward, Adv. Mater. **13**, 227 (2001).

[33] D. E. Henn, W. G. Williams, and D. J. Gibbson, J. Appl. Crystallogr. **4**, 256 (1971).

[34] A. D. Novaco and J. P. McTague, Phys. Rev. Lett. **38**, 1286 (1977).